HHS Public Access

Author manuscript

Magn Reson Med. Author manuscript; available in PMC 2021 May 01.

Published in final edited form as:

Magn Reson Med. 2020 May ; 83(5): 1760–1773. doi:10.1002/mrm.28031.

CEST MRI quantification procedures for breast cancer treatment-related lymphedema therapy evaluation

Rachelle Crescenzi[a,*], **Paula M. C. Donahue**[b,c], **Helen Mahany**[a], **Sarah K. Lants**[a], **Manus J. Donahue**[a,d,e]

[a]Department of Radiology, Vanderbilt University Medical Center, Nashville, TN, USA

[b]Physical Medicine and Rehabilitation, Vanderbilt University Medical Center, Nashville, TN, USA

[c]Vanderbilt Dayani Center for Health and Wellness, Nashville, TN, USA

[d]Department of Psychiatry, Vanderbilt University Medical Center, Nashville, TN, USA

[e]Department of Neurology, Vanderbilt University Medical Center, Nashville, TN, USA

Abstract

Purpose: To quantify CEST contrast in upper extremities of participants with lymphedema before and after standardized lymphatic mobilization therapy, using correction procedures for B_0 and B_1 heterogeneity, and T_1 relaxation.

Methods: Females with (n=12) and without (n=17) breast cancer treatment-related lymphedema (BCRL) matched for age, and body-mass-index (BMI) were scanned at 3.0T MRI. B_1 *efficiency* and T_1 were calculated in series with CEST in bilateral axilla (B_1 amplitude=2μT, $\Delta\omega$=±5.5 ppm, slices=9, spatial resolution=1.8×1.47×5.5mm^3). B_1 dispersion measurements (B_1=1-3μT; increment=0.5μT) were performed in controls (n=6 arms in 3 subjects). BCRL participants were scanned pre- and post-manual lymphatic drainage (MLD) therapy. CEST amide proton transfer (APT) and nuclear Overhauser effect (NOE) metrics corrected for B_1 *efficiency* were calculated including proton-transfer-ratio (PTR'), $MTR'_{asymmetry}$, and apparent-exchange-dependent-relaxation (AREX'). Non-parametric tests were used to evaluate relationships between metrics in BCRL participants pre- vs. post-MLD (two-sided p<0.05 required for significance).

Results: B_1 dispersion experiments showed non-linear dependence of Z-values on B_1 *efficiency* in the upper extremities; PTR' showed <1% mean fractional difference between subject-specific and group-level correction procedures. PTR'_{APT} significantly correlated with T_1 (Spearman's rho=0.57, p<0.001) and BMI (Spearman's rho=−0.37, p=0.029) in controls, and lymphedema stage (Spearman's rho=0.48, p=0.017) in BCRL participants. Following MLD therapy, PTR'_{APT} significantly increased in the affected arm of BCRL participants (pre- vs. post-MLD: 0.41±0.05 vs. 0.43±0.03, p=0.02) consistent with treatment effects from mobilized lymphatic fluid.

[*]**Corresponding Author:** Rachelle Crescenzi, PhD, Assistant Professor, Department of Radiology, Vanderbilt University Medical Center, 1161 21st Ave South, Nashville, TN, 37232, rachelle.crescenzi@vumc.org.

Declaration of conflict of interest: M.J.D. receives research related support from Philips North America and is the CEO of biosight, LLC which provides healthcare technology consulting services.

Conclusion: CEST metrics, following appropriate correction procedures, respond to lymphatic mobilization therapies and may have potential for evaluating treatments in participants with secondary lymphedema.

Introduction

Lymphatic and lymphoid tissue dysfunction is central to many pressing healthcare challenges of the 21st century, including infection and cellulitis[1], human immunodeficiency viral reservoirs[2], cancer metastasis[3] and lymphedema secondary to lymph node removal for cancer staging[4]. Breast cancer treatment-related lymphedema (BCRL) alone affects 300,000 participants annually in the United States and is a chronic, lifelong condition with a high mean two-year incidence of 30% in cancer survivors treated with lymph node dissection[5]. The underlying mechanism of *clinical* BCRL is well-characterized: when lymphatic transport capacity exceeds lymphatic load, protein-rich fluid accumulates in the interstitium, and macroscopic swelling, or lymphedema, results. However, there is more uncertainty regarding *sub-clinical* mechanisms: why only some participants develop lymphedema, whether surgical practices can be adapted to reduce incidence, and how emerging pharmacological or surgical interventions impact lymphatics[6]. Understanding these issues will require improved imaging methods to visualize anatomical and molecular characteristics of tissue health in the presence of overt and sub-clinical lymphatic dysfunction.

It is logical that lymphatic vascular insufficiency leads to altered dependent-tissue composition that can be quantified using quantitative imaging. Recently measurements of magnetic relaxation times of lymphatic fluid in vitro[7] and lymph nodes in vivo[8] have been reported, and this information has been applied to develop MRI techniques with enhanced sensitivity to lymphatic circulation[7-12].

An underexplored MRI contrast mechanism in lymphatic imaging is chemical exchange saturation transfer (CEST), which can provide metrics of proton exchange rate and associated macromolecular content when appropriately acquired and quantified. CEST MRI should have sensitivity to the protein-rich interstitial microenvironment present in the affected limbs of participants with BCRL, and could serve as a useful in vivo biomarker of lymphatic dysfunction. In support of this, previous work demonstrated the sensitivity of the amide proton transfer (APT) CEST effect for distinguishing lymphatic impairment asymmetry between the upper extremities of participants with unilateral BCRL[11].

While this prior study demonstrated feasibility, the challenges for CEST imaging in the upper extremities were not fully addressed, including appropriate procedures to reduce errors from static and transmit field heterogeneity in this problematic region, spin relaxation effects, and quantification procedures. For instance, upper extremity MRI over a bilateral field-of-view (generally 400 mm in the right/left direction) is especially challenged by B_0 and B_1 inhomogeneity in regions of interest lateral to the scanner isocenter. These challenges are particularly important to overcome when comparing CEST metrics longitudinally after treatment intervention. One of the most common therapies for BCRL is manual lymphatic drainage (MLD), which is known to temporarily mobilize lymph stasis

from superficial tissues into deeper lymphatic channels. If CEST metrics are to aid evaluation of emerging lymphatic therapies, it is logical to first evaluate whether CEST is sensitive to expected changes following this standardized intervention.

The focus of this study, therefore, is to quantify CEST metrics in upper extremities before and after MLD therapy in participants with BCRL. In order to compare CEST measurements longitudinally, we outline a CEST MRI protocol for the upper extremities and procedures for correcting the static (B_0) and transmit (B_1) field heterogeneity and T_1 relaxation effects. After appropriate corrections, CEST outcome metrics including proton transfer ratio (*PTR*), asymmetric magnetization transfer ratio ($MTR_{asymmetry}$), and the apparent exchange-dependent relaxation (*AREX*)[13] are quantified in healthy females, and in participants with BCRL before and immediately after MLD therapy. Results are intended to report methods for a free-breathing, clinically feasible upper extremity CEST protocol, establish how this contrast varies between participants with and without known lymphatic dysfunction, and to evaluate the potential of CEST imaging for quantifying changes in tissue environment secondary to lymphatic mobilization.

Methods

Volunteer criteria

All participants provided informed, written consent in accordance with the Vanderbilt University Institutional Review Board and were enrolled as part of the prospective clinical trial: Imaging Noninvasively with Functional-MRI for Onset, Response and Management of Lymphatic Impairment (INFORM^{LI}, ClinicalTrials.gov Identifier:). The study cohort (n=29; sex=female; handedness=right) consisted of participants with unilateral BCRL (n=12) or control participants with no history of chronic lymphatic insufficiency (n=17). BCRL participants had at least one axillary lymph node removed as part of standard-of-care breast cancer treatment at least one month prior to imaging to allow for residual surgical swelling to reduce. BCRL participants were not actively receiving chemotherapy or radiation treatment. Control participants were matched for sex, age, and body-mass-index (BMI) to the BCRL group and did not have a history of cancer or lymph node removal.

Physical exam and manual lymphatic drainage therapy

Prior to imaging, all participants underwent a physical exam for measurement of height and weight for calculation of BMI. In BCRL participants, information regarding number of lymph nodes removed, lymphedema stage, and lymphedema location (right or left arm, torso, and/or upper quadrant) were determined by a physical therapist (P.M.C.D.) with Lymphedema Association of North America (LANA) certification, and 12 years of experience treating participants with lymphedema. To evaluate the sensitivity of CEST to changes in tissue composition following a standardized intervention, BCRL participants underwent a 50-minute session of MLD therapy; imaging was performed before (pre-MLD) and immediately after (post-MLD) a single session of MLD. MLD stimulated lymphatic fluid flow from the affected limb and upper quadrant toward the ipsilateral lower quadrant and contralateral upper quadrant to aid in reabsorption.

MRI experiments

All participants received CEST imaging as part of a multi-modal MRI exam. Volunteers were positioned supine with arms at their sides and scanned at 3.0T (Philips Achieva, Best, The Netherlands) using body coil radiofrequency transmission and 16-channel torso coil reception. A torso coil was chosen to achieve bilateral coverage of the right and left arms.

First, for subsequent slice planning, multi-point T_1-weighted Dixon imaging was applied (dual-echo per TR=3.5 ms, TE_1=1.15, TE_2=2.3 ms, 3D gradient echo readout; duration=18s) over a bilateral field-of-view (FOV= 520×424×192 mm^3, spatial resolution=0.9×0.74×2.5 mm^3) centered on the axilla (Figure 1a-b) and without a shutter radius to allow for this large FOV to be evaluated. Axillary regions were imaged separately using a reduced FOV (180×180×50 mm^3) for higher spatial resolution T_2-weighted imaging with fat-suppression (spectral attenuated inversion recovery, SPAIR, TR/TE=3500/60 ms, spatial resolution=0.3×0.3×5 mm^3, Figure 1c).

Next, imaging experiments to measure B_1 *efficiency*, T_1 relaxation time, and CEST metrics were performed in the upper extremities at the level of the axillary lymph nodes. Shared geometrical imaging parameters for these sequences were: FOV= 520×424×49 mm^3, spatial resolution=1.8×1.47×5.5 mm^3, slices=9, Figure 1d-g. Automated shimming routines were performed over a selective volume, and the volume-specific water resonance was manually chosen using the vendor (Philips)-supplied interactive frequency (F0) selection option; the proton peak with the higher ppm is selected, corresponding to water resonance. This procedure is especially important in large participants in whom the fat signal can be large compared to the water signal. For mapping B_1 *efficiency*, a dual-TR approach was utilized (TR_1=30 ms, TR_2=130 ms, flip angle FA=60 degrees, 3D gradient echo). Longitudinal relaxation time (T_1) mapping was achieved using the multi-flip angle (FA=20, 40, 60 degrees, TR/TE = 100/4.6 ms, 3D gradient echo) method which does not rely on inversion or saturation of the signal[14]. The total scan duration for B_1 mapping was 1 min 42s, and for T_1 mapping was 3 min 12s.

CEST was performed over an identical FOV as B_1 and T_1 mapping acquisitions, and without resetting the B_1 calibration. First, to evaluate B_1 correction procedures, in a subset of control volunteers (n=3), B_1 mapping and CEST imaging procedures were repeated during the same scan session with prescribed B_1 amplitudes (1, 1.5, 2, 2.5, and 3 μT), representing 50-150% of the nominal B_1 amplitude of 2 μT. B_1 dispersion curves were used for subsequent correction procedures as outlined below.

In all volunteers CEST was performed using a frequency selective sinc-windowed gaussian saturation pulse (prescribed B_1 amplitude=2 μT, saturation pulse duration=75 ms) followed by a multi-slice echo planar imaging (EPI) readout (EPI factor=7, TR/TE=155/8.3). The sequence was repeated for an array of saturation frequencies (offset from water resonance $\Delta\omega$=±5.5 ppm) with asymmetric sampling increments of 0.2 ppm in the range $\Delta\omega$=5.5 to −1.0 ppm, and increments of 0.4 ppm in the range $\Delta\omega$=−1.0 to −5.5 ppm. Six additional dynamics were acquired with a frequency offset sufficiently far from water resonance ($\Delta\omega$=80,000 Hz) to measure magnetization in the absence of major chemical exchange effects. This acquisition scheme was chosen to oversample the exchanging resonance of

interest (e.g., amide protons at approximately 3.5 ppm) while maintaining a clinically-feasible scan time. The power and duration were chosen to additionally render this sequence clinically relevant in the presence of common MR conditional implants in this region including titanium ports and biopsy clips. Total duration for CEST was 6 min.

B_1 and T_1 mapping

Quantitative B_1 *efficiency* and T_1 maps were calculated using custom routines in Matlab (R2015b, Mathworks, Natick, MA). The B_1 *efficiency* map (units of ratio) was calculated from the dual-TR acquisition according to methods reported by Yarnykh[15]. The T_1 relaxation time (units of seconds) was derived from multi-flip angle acquisitions corrected for B_1 *efficiency* according to Wang *et al.*[14] Briefly, the slope of a least-squares linear fit was determined for,

$$\frac{SI_{\theta,meas}}{\sin(\theta_{abs})} = \frac{SI_{\theta,meas}}{tan(\theta_{abs})} \cdot exp^{-\frac{TR}{T1}} + C \qquad \text{eqn. [1]}$$

where ($SI_{\theta,meas}$) is the measured signal intensity acquired at three nominal flip angles, θ_{abs} is the absolute flip angle determined by multiplying the prescribed flip angle by the B_1 *efficiency*, and C is a constant. Note that a plot of $SI_{\theta,meas}/\sin(\theta_{abs})$ vs. $SI_{\theta,meas}/\tan(\theta_{abs})$ provides a slope of $e^{-TR/T1}$, from which T_1 is calculated.

CEST B_0 and B_1 correction

The purpose of this component of the study was to understand how field inhomogeneity correction and different CEST quantification procedures influence sensitivity of CEST to the effects of MLD therapy. Multiple metrics of the CEST effect can be calculated from a commonly-considered normalized signal intensity, or Z-spectrum, defined as,

$$Z(\Delta\omega) = S_{sat}(\Delta\omega) \,/\, S_0, \qquad \text{eqn. [2]}$$

where $Z(\Delta\omega)$ is the fractional signal (S_{sat}) from a frequency-selective saturation ($\Delta\omega$ relative to water) RF pulse normalized by the equilibrium magnetization signal in the absence of RF pre-saturation (S_0)[16]. The associated Z-spectrum was calculated over an array of RF pre-saturation frequency values ($\Delta\omega$=±5.5 ppm). $Z(\Delta\omega)$ is dependent on accurate frequency referencing, although may be biased by static (ΔB_0) and transmit (ΔB_1) field heterogeneity as discussed below. In upper extremities where both B_0 and B_1 vary spatially, corrections procedures must be considered to improve fidelity of the CEST metric.

The Z-spectrum data were interpolated (smooth spline interpolation with factor of 3) to 111 offset frequencies between ±5.5 ppm with step size of 0.1 ppm. To correct for ΔB_0, the minimum point was found and the interpolated Z-spectrum shifted such that the minimum Z-value occurs at 0 ppm; voxels in which spectra have multiple minima or requiring ΔB_0 greater than 2 ppm were discarded and were typically located in lung cavities. A separate acquisition using the water saturation shift referencing (WASSR) method is often used for B_0 correction[17], which is also a valid approach, however WASSR requires additional scan

time, and may not reflect the temperature and frequency drift of the scanner during the CEST scan.

Following B_0 correction, Z-values preserved for CEST quantification related to lymphedema were calculated and were (i) Z_{APT} defined as the mean $Z(\Delta\omega)$ from the amide proton transfer (APT) effect: $\Delta\omega_{APT}$ = 3 to 4 ppm, and (ii) Z_{NOE} defined as the magnetization transfer due to the nuclear Overhauser effect (NOE): $\Delta\omega_{NOE}$ = −3 to −4 ppm.

Finally, Z-values corresponding to the APT and NOE effects were corrected for B_1 *efficiency* based on measurement of the tissue-specific B_1-dependence of CEST contrast, as previously demonstrated in brain tissue[18-20]. A second-order polynomial fit was applied using,

$$Z(\Delta\omega, B_1)\,|_{\Delta\omega APT,\,\Delta\omega NOE} = p_2 {B_1}^2 + p_1 B_1 + p_0, \qquad \text{eqn. [3]}$$

where $Z(\Delta\omega, B_1)$ was evaluated separately for $\Delta\omega$ over the APT or NOE range, as defined above. B_1 is the transmit magnetic field, and p_0, p_1, and p_2 are coefficients of the polynomial fit.

When eqn. [3] is evaluated at the nominal B_1, B_{1nom}=2 μT and separately at the relative B_1, B_{1rel}=B_{1nom}·B_1*efficiency*, a correction factor can be derived for any range of $\Delta\omega$,

$$\Delta Z(\Delta\omega, B_1) = Z(\Delta\omega, B_{1nom}) - Z(\Delta\omega, B_{1rel})\,. \qquad \text{eqn. [4]}$$

Thus, B_1-corrected Z'_{APT} and Z'_{NOE} were calculated for the measured B_1 *efficiency* according to,

$$Z'(\Delta\omega, B_1)\,|_{\Delta\omega APT,\,\Delta\omega NOE} = [Z(\Delta\omega) + \Delta Z(\Delta\omega, B_1)]_{\Delta\omega APT,\,\Delta\omega NOE}\,. \qquad \text{eqn. [5]}$$

In our nomenclature, the addition of the ′ superscript denotes a B_1-corrected metric. The intercept at B_1=0 (p_0 term) was constrained to one similar to previous implementations of this method[19], and is not relevant to quantification as it is subtracted out of eqn. 4. Polynomial coefficients for Z'_{APT} and Z'_{NOE} were calculated in the left and right arm muscle of three volunteers, and the generalizability of this correction factor was evaluated in this study.

CEST quantification

The CEST effect due to APT and NOE exchange mechanisms can be quantified using the B_1-corrected Z values, Z'_{APT} and Z'_{NOE}. We first calculated the corrected proton transfer ratio (PTR') that is directly proportional to the amount of exchangeable protons for constant pH and temperature,

$$PTR'_{APT} = 1 - Z'_{APT}, \qquad \text{eqn. [6]}$$

and

$$PTR'_{NOE} = 1 - Z'_{NOE}. \quad \text{eqn. [7]}$$

Since the PTR contains additional contributions from spillover of direct saturation and broad magnetization transfer, the asymmetry of the MTR was calculated as

$$MTR'_{asymmetry} = Z'_{NOE} - Z'_{APT}. \quad \text{eqn. [8]}$$

PTR is additionally proportional to the T_1 relaxation time of tissue[16]. The metric AREX reduces T_1 dependence of the CEST effect and is derived from the inverse z-spectrum[21]. Here we calculated AREX according to,

$$AREX' = \left| \frac{1}{Z'_{APT}} - \frac{1}{Z'_{NOE}} \right| / T_1, \quad \text{eqn.[9]}$$

using Z'_{NOE} as the reference value, and T_1 was measured from an identical region.

Image rendering and parameter calculations in regions of interest

Voxel-wise calculations were performed for B_1, T_1, PTR_{APT}, and PTR'_{APT} and parameter maps rendered in Matlab using the “RdYlBu” colorblind-friendly colormap reversed from ColorBrewer (brewermap.m)[22].

Imaging metrics preserved for hypothesis testing were calculated in regions of interest (ROI) segmented from the left and right arms on the T_1-weighted image (Figure 1b) and guided by the high spatial resolution T_2-weighted image (Figure 1c). The ROI included the medial arm muscle spanning three consecutive slices in the foot-head direction, centered at the approximate level of the crest of the greater tubercle. The mean Z-spectrum was calculated from each ROI (eqn. 2), and identical ROIs were applied to B_1 and T_1 maps. The corresponding B_1 correction factor was applied to Z_{APT} and Z_{NOE} according to the B_1 *efficiency* measured within the ROI (eqns. 3-5). CEST metrics (i) PTR'_{APT}, (ii) PTR'_{NOE}, (iii) $MTR'_{asymmetry}$, and (iv) $AREX'$ were calculated from Z'_{APT} and Z'_{NOE} in the ROIs (eqns. 6-9). These B_1-corrected CEST and T_1 parameters were preserved for hypothesis testing.

Statistical analysis

The statistical objectives of this study were to (i) calculate B_1 correction factors for Z-spectra obtained in the upper extremities, (ii) quantify the relationships between B_1-corrected CEST metrics and T_1 relaxation time in this region, as well as relationships between these metrics and demographic and disease risk factors, and (iii) evaluate whether corrected CEST metrics provide contrast changes consistent with lymphatic mobilization induced by MLD therapy.

First, subject-specific correction factors were calculated from B_1 dispersion curves in left and right arms of 3 participants. A group-mean correction factor was also calculated as the mean of the coefficients (p_1, p_2 of a second order polynomial fit, eqn. [3]) of all six arms. In

each of six regions, the subject-specific and group-mean B_1-corrected factors were presented as mean +/− standard deviation, and fractional differences between methods calculated.

Second, the group-mean B_1 correction factors were applied to the control and BCRL dataset. To evaluate relationships between imaging metrics in the upper-extremities, we considered data from right and left arms of controls and participants with BCRL measured before and after therapy (n=82 observations). The Spearman's rank correlation coefficient was calculated between pairs of CEST metrics: PTR'_{APT}, PTR'_{NOE}, $MTR'_{asymmetry}$ and $AREX'$ (ratio), and between CEST metrics and the T_1 relaxation time. To understand how these parameters varied in the absence of pathology, Spearman's tests were applied in control data (n=34 observations, left and right arms) to quantify relationships between the imaging metrics PTR'_{APT}, $AREX'$, and T_1 relaxation time and BMI or age. To understand how these parameters varied with clinical indicators of disease in BCRL participants (n=24 observations, pre-MLD affected and contralateral arms), Spearman's tests were applied in pre-MLD BCRL patient data to identify potential relationships between imaging metrics and BCRL stage or number of lymph nodes removed.

Third, we quantified (i) whether imaging metrics are discriminatory for BCRL disease classification, and (ii) which CEST metrics adjust after lymphatic mobilization with MLD. To test for potential differences in study parameters between independent samples from controls and participants with BCRL, the Wilcoxon rank sum test was used. To test for potential differences in study parameters between dependent samples from affected and contralateral arms of participants with BCRL, and between metrics pre- and post-MLD, the Wilcoxon signed rank test was used.

In all cases, a two-sided p-value<0.05 was required for significance.

Results

Participants with BCRL (age=52.3±10.7 years, age range=33–77 years; BMI=30.5±7.0 kg/m^2, BMI range=21.6-45.5 kg/m^2, 100% right-hand dominant) and female controls (age=44.1±15.2 years, age range=23–73 years; BMI=27.6±6.2 kg/m^2, BMI range=19.6-39.9 kg/m^2, 94% right-hand dominant) matched for age (p=0.09) and BMI (p=0.27) met inclusion criteria. Participants with (stage 1 or 2) or at risk (stage 0) for BCRL (stage=1.33±0.89, stage range=0-2) had lymph nodes dissected or removed (number of lymph nodes=17.6±6.3, range=5-27) from their right (n=8) or left (n=4) arms for the purpose of breast cancer staging. Additionally, 75% of participants received radiation treatment to the affected axilla, 33% received neo-adjuvant chemotherapy, and 100% received adjuvant chemotherapy (Table 1).

B_1 dispersion of Z in the upper extremities

For these CEST sequence parameters applied at 3.0T in the deep muscle of the upper extremities, the group-mean coefficients of a second-order polynomial fit for $Z_{APT}(B_1)$ were p_2=−0.0039±0.0098 and p_1=−0.1810±0.0441; coefficients for $Z_{NOE}(B_1)$ were found to be p_2=0.0026±0.0139 and p_1=−0.1942±0.0544 (Figure 2). B_1 correction that applied subject-specific versus group-mean correction factors were in close agreement for all six arms tested

(Figure 3). When applying the subject-specific correction, PTR'_{APT} and PTR'_{NOE} were adjusted by 7.1±8% and 6.8±8% respectively; the group-mean correction adjusted PTR'_{APT} and PTR'_{NOE} similarly by 8.1±10% and 7.7±10% respectively. Given the small discrepancy between PTR metrics using subject-specific vs. group-mean correction factors (PTR'_{APT} mean fractional difference=0.82±2%, PTR'_{NOE} mean fractional difference=0.69±2%), the group-mean coefficients were used for B_1 correction procedures.

Relationship between imaging metrics

We observed a significant, positive relationship between T_1 and B_1-corrected CEST metrics among all participant scans (n=82 observations) PTR'_{APT} (Spearman's rho=0.57, $p<0.001$, Figure 4a) and PTR'_{NOE} (Spearman's rho=0.58, $p<0.001$). $AREX'$ demonstrated a weaker, inverse relationship with T_1 relaxation time ($AREX'$ vs. T_1, Spearman's rho=−0.21, $p=0.06$, Figure 4b) as did $MTR'_{asymmetry}$ vs. T_1 (Spearman's rho=−0.22, $p=0.05$).

Among CEST metrics, PTR'_{APT} was statistically unrelated to $MTR'_{asymmetry}$ (Spearman's rho=0.08, $p=0.45$, Figure 4c), as was PTR'_{APT} and $AREX'$ (Spearman's rho=0.07, $p=0.51$). A significant, positive relationship was observed between $AREX'$ and $MTR'_{asymmetry}$ (Spearman's rho=0.99, $p<0.001$, Figure 4d), and between PTR'_{APT} and PTR'_{NOE} (Spearman's rho=0.79, $p<0.001$). Additional summary information for imaging metrics is provided in Supporting Information Table S1.

Relationship between imaging metrics, demographics, and clinical risk factors

Among healthy female participants (n=34 observations, left and right arms), there was a significant inverse relationship between BMI and PTR'_{APT} (Spearman's rho=−0.37, $p=0.029$) and $AREX'$ (Spearman's rho=−0.36, $p=0.036$). There was no relationship between any CEST metric with age, and there was no relationship between T_1 and age or BMI (Table 2).

Among participants with BCRL (n=24 observations, pre-MLD affected and contralateral arms), a significant relationship between PTR'_{APT} and BCRL stage (Spearman's rho=0.48, $p=0.017$) was observed. There was no relationship between imaging metrics and number of lymph nodes removed in participants with BCRL (Table 2).

Imaging metrics in healthy females and participants with BCRL

The mean T_1 was similar in the left and right arms of healthy female control participants (left T_1=1.67±0.28s, right T_1=1.71±0.38s, $p=0.73$). In participants with BCRL, T_1 was not significantly different between affected and contralateral arms (affected T_1=1.43±0.26s, contralateral T_1=1.54±0.24s, $p=0.28$). Compared to female controls, T_1 relaxation time was significantly reduced in the affected arms of participants with BCRL ($p=0.009$, Figure 5a).

PTR'_{APT} was similar between left and right arms of healthy female controls (in units of ratio; left PTR'_{APT}=0.41±0.07, right PTR'_{APT}=0.42±0.03, $p=0.40$). In BCRL participants, PTR'_{APT} was not significantly different between the affected and contralateral arms (affected PTR'_{APT}=0.41±0.05, contralateral PTR'_{APT}=0.42±0.04, $p=0.36$, Figure 5b). PTR'_{NOE} was not significantly different between the affected and contralateral arms (affected

PTR'_{APT}=0.40±0.05, contralateral PTR'_{APT}=0.42±0.06, p=0.54, Figure 5c). We observed a trend for higher $AREX'$ in the affected arms (0.008±0.04, p=0.16) and contralateral arms (0.009±0.05, p=0.23) of BCRL participants compared to controls (−0.011±0.04, Figure 5d). Together these results demonstrate differences in T_1 relaxometry to the deep arm muscle in participants with BCRL, however after correcting for B_0, B_1, and T_1 there was no statistically significant difference with the stated criteria for CEST metrics in the affected arm of participants with BCRL.

Effect of MLD therapy on imaging metrics in BCRL participants

Following MLD therapy, a trend for increased T_1 was measured in the affected arms (1.72±0.46, p=0.06), but not contralateral arms (1.62±0.40, p=0.42), compared to the pre-MLD T_1 measurement (Figure 5a). PTR'_{APT} significantly increased following MLD in the affected arms (pre-MLD PTR'_{APT}=0.41±0.05, post-MLD PTR'_{APT}=0.43±0.03, p=0.02) but not contralateral arms (pre-MLD PTR'_{APT}=0.42±0.04, post-MLD PTR'_{APT}=0.42±0.04, p=0.68, Figure 5b). PTR'_{NOE} significantly increased following MLD in the affected arms (pre-MLD PTR'_{NOE}=0.40±0.05, post-MLD PTR'_{NOE}=0.44±0.03, p=0.03) but not contralateral arms (pre-MLD PTR'_{NOE}=0.42±0.06, post-MLD PTR'_{NOE}=0.41±0.05, p=0.67, Figure 5c). No significant effect of MLD on $AREX'$ was measured in the affected arms (pre-MLD $AREX'$=0.008±0.04, post-MLD $AREX'$=−0.006±0.06, p=0.51) or contralateral arms (pre-MLD $AREX'$=0.009±0.05, post-MLD $AREX'$=0.01±0.08, p=0.96) compared to pre-MLD measurement (Figure 5d).

Increased PTR'_{APT} was observed in the majority of BCRL participants on the affected side but not the contralateral side (Figure 6). A case-example of a participant with stage 0 BCRL is presented in which PTR'_{APT} after B_1-correction is enhanced on the affected side following MLD therapy (Figure 7). These results demonstrate the sensitivity of PTR'_{APT} and PTR'_{NOE}, and to a lesser extent T_1 relaxometry, to MLD lymphatic mobilization therapy.

Discussion

The focus of this study was to determine the sensitivity of a clinically-feasible CEST imaging protocol for detecting treatment effects in participants with lymphedema of the upper extremities where field inhomogeneity confounds CEST quantification. To evaluate whether expected mobilization of proteinaceous lymph stasis into deeper tissues by MLD therapy is detectable by CEST, we employed the latest methods for correcting CEST metrics for B_0 and B_1 inhomogeneities before and after therapy, and also considered $AREX$ to compensate for T_1 relaxation enhancement of the CEST effect.

Technical considerations

We report in the upper extremities for the first time the dependence of CEST Z-spectra on transmit field B_1 efficiency in the arm muscle in healthy females. The dependence of Z on B_1 is tissue-specific and necessitates in vivo evaluation for each application of CEST imaging, as previously demonstrated[18,19]. Thus, strategies that employ empirically-derived B_1 correction factors for CEST imaging at 3.0T MRI may be used in the upper extremities in

future applications, although must be evaluated for each sequence and requires measurement of B_1 efficiency with each CEST acquisition.

Next, relationships between B_1-corrected CEST metrics and T_1 revealed a direct correlation between PTR' and T_1, whereas $AREX'$ appeared largely independent of T_1, as expected although this has not been previously evaluated in the upper extremities. These data are consistent with previous empirical and theoretical demonstrations that PTR depends on T_1 in the region of interest[16,23]. $AREX$ was found to correlate closely with $MTR_{asymmetry}$, while $AREX$ has the added benefit of reduced dependence on T_1[21]. Compared to $MTR_{asymmetry}$, $AREX$ has a broader dynamic range and increased variability due to noise propagation inherent in the T_1 correction procedure. Additional errors may be introduced in the $AREX$ calculation when the spin system is not in steady-state, which is always a concern in regions with higher field inhomogeneity and as has been investigated in detail in the literature[21].

An inverse correlation was found between PTR'_{APT} and BMI among healthy females. There could be physiologic reasons for this trend, or artifactual. CEST imaging in the body is typically confounded by direct saturation of fat signal in the range of −3 to −4 ppm, creating a pseudo-NOE signal in tissues with higher fat content[24]. Although fat suppression was applied in the preparation module of the CEST sequence, methods to adequately separate direct saturation of fat could be achieved using a Dixon readout sequence, similar to CEST applications reported in the breast[25,26]. Still, the observed trend with PTR'_{APT} indicates a physiologic decrease in labile macromolecules in the setting of obesity (mean BMI of this cohort is overweight), that could be the topic of further exploration.

Consistency with clinical indicators of disease

The significant clinical findings of this study are (i) a positive relationship exists between PTR'_{APT} and lymphedema stage, (ii) shorter T_1 in the affected upper extremities of participants with BCRL compared to female controls, and (iii) greater PTR'_{APT} and PTR'_{NOE} effects in the deep tissue of affected but not contralateral limbs of participants with BCRL following MLD therapy to affected limbs.

The CEST metric PTR'_{APT} demonstrated a significant positive correlation with BCRL stage. This finding is consistent with a previous report[27] and the biological explanation that higher amounts of edema and protein content in limbs affected by higher BCRL stages yields a larger APT CEST effect. There was no observed relationship between imaging metrics and number of lymph nodes removed in the local axilla of participants with BCRL, which underscores the discrepancy between lymph node removal procedures and disease severity[28].

Shorter T_1 in the tissue of BCRL participants is consistent with the presence of hardened fibrotic tissue that can develop as a result of long-standing lymphedema. Similar tissues with cross-linked collagen experience reduced T_1 relaxation[29]. Fatty infiltration of the deep muscle is also common in lymphedema[30], with similar impact on T_1 relaxation. The majority of participants in this study (8 out of 12 participants) were determined to have stage 2 lymphedema characterized by hypertrophic subcutaneous adipose and fibrotic tissue in the affected arm and upper quadrant. Additional radiation treatments received by 75% of

participants are known to induce fibrosis[31]. Imaging biomarkers that can reveal the onset of fibrosis are highly relevant for informing the clinical need for aggressive treatment intervention to prevent or minimize progression[32-34]. T_1 relaxation time mapping with correction for B_1 inhomogeneities should be further investigated for sensitivity to lymphedema and fibrosis onset, whereas CEST imaging may provide sensitivity to the effects of therapy, as we will discuss next.

Prior to MLD therapy, apparent differences in CEST signal in the affected versus contralateral arm may not be realized because the bilateral effects of many systemic cancer therapies will alter tissue health in both limbs, and therefore the contralateral limb is not strictly a healthy reference region. Following MLD, increased PTR'_{APT} and PTR'_{NOE} in the deep arm muscle is consistent with the therapeutic mechanism, whereby mobilizing superficial lymphatic congestion in the skin and interstitial tissue manually directs edematous fluid into the deeper subcutaneous tissues for uptake through additional reabsorption pathways[35-37]. The source of APT pool in the muscle consists of macromolecules in the tissue parenchyma. Demonstrated mechanisms of increased blood flow to the muscle following MLD therapy[38,39] may also enhance the APT pool in the muscle.

The macromolecule component of edematous fluid consists of a substantial amount of lipoproteins[40], some of which have exchangeable protons through NOE mechanisms[24]. Roughly 50% of lipoproteins are processed through the lymphatic vasculature and extracellular space[41], and should be considered when tailoring MRI sequences for lymphatic pathophysiology. Although the source of NOE signal remains unknown in human conditions of lymphedema or cancer, recent studies highlight NOE enhancement in the condition of glioblastoma tumors[42-44]. The NOE signal is additionally sensitive to tissue pH, temperature, and oxygenation status in preclinical studies of cancer[45,46], and is an interesting area of investigation.

Limitations

BCRL participants in this study represent typical breast cancer survivors who undergo varying amounts of neoadjuvant and adjuvant chemotherapy, as well as radiation treatments, that prevents a comparison between participants undergoing identical lymphedema treatments. To address this limitation, we focused on scanning a bilateral FOV in order to evaluate the effects of MLD therapy on unilateral lymphedema using the contralateral tissue as an internal control region. Additionally, this study demonstrates a nearly symmetric Z-spectrum in the APT and NOE ranges; consequently the magnitude of asymmetry metrics, $AREX'$ and $MTR'_{asymmetry}$, was small. Our analysis has not ruled out the possibility of contributions from the semi-solid MT pool in participants with lymphedema or following MLD therapy. Such MT signal could arise from fatty-fibrosis tissue that often deposits subcutaneously in participants with advanced lymphedema. We anticipate the MT signal would be sensitive to differences in affected limbs with advanced lymphedema and fibrosis, and insensitive to changes in tissue composition following MLD. This is because MLD is a superficial skin-stretch that is not intended to mobilize deep collagen directly, where we report the sensitivity of CEST metrics. It is possible that in participants with advanced

lymphedema, superficial sub-dermal fibrosis may soften with application of MLD; however, this trend would suggest a reduction of the semi-solid MT effect, which is inconsistent with our findings. Rather, we find evidence of increased water T_1 in deep tissues following MLD, consistent with relocation of lymphatic fluid associated with increased concentration of amide protons. Further analysis could apply multi-pool proton exchange models to better understand the relative contributions from MT and CEST in the setting of lymphedema.

Conclusion

We provide a clinically-feasible free-breathing 3.0T protocol for measuring CEST effects in bilateral upper extremities of participants with BCRL. Our results demonstrate the feasibility of empirically correcting CEST metrics for B_1 efficiency in the upper extremities. When these appropriate considerations are taken into account, study results demonstrate that the APT and NOE proton transfer ratio can be used to visualize the effect of lymphatic mobilization therapies, which are known to mobilize proteinaceous fluid into deep tissues. As BCRL represents the most common, chronic comorbidity associated with breast cancer treatment, methods could motivate using CEST as a new tool to evaluate emerging pharmacological and physical therapy techniques in this population.

Supplementary Material

Refer to Web version on PubMed Central for supplementary material.

Acknowledgments

Funding: NIH/NINR: 1R01NR015079, Lipedema Foundation postdoctoral fellowship, Lipedema Foundation Collaborative Award (#12)

References

1. Pallin DJ, Camargo CA Jr. & Schuur JD Skin infections and antibiotic stewardship: analysis of emergency department prescribing practices, 2007-2010. The western journal of emergency medicine 15, 282–289, doi:10.5811/westjem.2013.8.18040 (2014). [PubMed: 24868305]
2. Tawakol A et al. Association of Arterial and Lymph Node Inflammation With Distinct Inflammatory Pathways in Human Immunodeficiency Virus Infection. JAMA Cardiol 2, 163–171, doi:10.1001/jamacardio.2016.4728 (2017). [PubMed: 27926762]
3. Karaman S & Detmar M Mechanisms of lymphatic metastasis. J Clin Invest 124, 922–928, doi:10.1172/JCI71606 (2014). [PubMed: 24590277]
4. Rockson SG Lymphedema after Breast Cancer Treatment. N Engl J Med 380, 694, doi:10.1056/NEJMc1817537 (2019).
5. DiSipio T, Rye S, Newman B & Hayes S Incidence of unilateral arm lymphoedema after breast cancer: a systematic review and meta-analysis. Lancet Oncol 14, 500–515, doi:10.1016/S1470-2045(13)70076-7 (2013). [PubMed: 23540561]
6. Alitalo K The lymphatic vasculature in disease. Nature medicine 17, 1371–1380, doi:10.1038/nm.2545 (2011).
7. Rane S et al. Clinical feasibility of noninvasive visualization of lymphatic flow with principles of spin labeling MR imaging: implications for lymphedema assessment. Radiology 269, 893–902, doi:10.1148/radiol.13120145 (2013). [PubMed: 23864103]
8. Crescenzi R et al. 3.0 T relaxation time measurements of human lymph nodes in adults with and without lymphatic insufficiency: Implications for magnetic resonance lymphatic imaging. NMR Biomed 31, e4009, doi:10.1002/nbm.4009 (2018). [PubMed: 30311705]

9. Korteweg MA, Z. J, van Diest PJ, van den Bosch MAAJ, Luijten PR, van Hillegersberg R, Mali WPThM, Veldhuis WB. Characterization of ex vivo healthy human axillary lymph nodes with high resolution 7 Tesla MRI. European Radiology 21, 310–317 (2011). [PubMed: 20694817]
10. Donahue PM et al. Bilateral Changes in Deep Tissue Environment After Manual Lymphatic Drainage in Patients with Breast Cancer Treatment-Related Lymphedema. Lymphatic Research and Biology 15, 45–56 (2017). [PubMed: 28323572]
11. Donahue MJ et al. Assessment of lymphatic impairment and interstitial protein accumulation in patients with breast cancer treatment-related lymphedema using CEST MRI. Magn Reson Med 75, 345–355, doi:10.1002/mrm.25649 (2016). [PubMed: 25752499]
12. Crescenzi R et al. Lymphedema evaluation using noninvasive 3T MR lymphangiography. J Magn Reson Imaging 46, 1349–1360, doi:10.1002/jmri.25670 (2017). [PubMed: 28245075]
13. Zaiss M & Bachert P Chemical exchange saturation transfer (CEST) and MR Z-spectroscopy in vivo: a review of theoretical approaches and methods. Phys Med Biol 58, R221–269, doi: 10.1088/0031-9155/58/22/R221 (2013). [PubMed: 24201125]
14. Wang J, Qiu M, Kim H & Constable RT T1 measurements incorporating flip angle calibration and correction in vivo. J Magn Reson 182, 283–292, doi:10.1016/j.jmr.2006.07.005 (2006). [PubMed: 16875852]
15. Yarnykh VL Actual flip-angle imaging in the pulsed steady state: a method for rapid three-dimensional mapping of the transmitted radiofrequency field. Magn Reson Med 57, 192–200, doi: 10.1002/mrm.21120 (2007). [PubMed: 17191242]
16. van Zijl PCM & Yadav NN Chemical exchange saturation transfer (CEST): What is in a name and what isn't? Magnetic Resonance in Medicine 65, 927–948, doi:10.1002/mrm.22761 (2011). [PubMed: 21337419]
17. Kim M, Gillen J, Landman BA, Zhou J & van Zijl PC Water saturation shift referencing (WASSR) for chemical exchange saturation transfer (CEST) experiments. Magn Reson Med 61, 1441–1450, doi:10.1002/mrm.21873 (2009). [PubMed: 19358232]
18. Singh A, Cai K, Haris M, Hariharan H & Reddy R On B1 inhomogeneity correction of in vivo human brain glutamate chemical exchange saturation transfer contrast at 7T. Magnetic Resonance in Medicine 69, 818–824, doi:10.1002/mrm.24290 (2013). [PubMed: 22511396]
19. Windschuh J et al. Correction of B1-inhomogeneities for relaxation-compensated CEST imaging at 7 T. NMR Biomed 28, 529–537, doi:10.1002/nbm.3283 (2015). [PubMed: 25788155]
20. Khlebnikov V et al. On the transmit field inhomogeneity correction of relaxation-compensated amide and NOE CEST effects at 7 T. NMR Biomed 30, doi:10.1002/nbm.3687 (2017).
21. Zaiss M et al. Inverse Z-spectrum analysis for spillover-, MT-, and T1 -corrected steady-state pulsed CEST-MRI--application to pH-weighted MRI of acute stroke. NMR Biomed 27, 240–252, doi:10.1002/nbm.3054 (2014). [PubMed: 24395553]
22. Cobeldick S (2014) ColorBrewer (Version 3.0.0.2) [brewermap.m]. https://www.mathworks.com/matlabcentral/fileexchange/45208-colorbrewer-attractive-and-distinctive-colormaps.
23. Li H et al. R1 correction in amide proton transfer imaging: indication of the influence of transcytolemmal water exchange on CEST measurements. NMR Biomed 28, 1655–1662, doi: 10.1002/nbm.3428 (2015). [PubMed: 26466161]
24. Lu J, Zhou J, Cai C, Cai S & Chen Z Observation of true and pseudo NOE signals using CEST-MRI and CEST-MRS sequences with and without lipid suppression. Magn Reson Med 73, 1615–1622, doi:10.1002/mrm.25277 (2015). [PubMed: 24803172]
25. Zhang S et al. CEST-Dixon for human breast lesion characterization at 3 T: A preliminary study. Magn Reson Med 80, 895–903, doi:10.1002/mrm.27079 (2018). [PubMed: 29322559]
26. Zhang S et al. Z-spectrum appearance and interpretation in the presence of fat: Influence of acquisition parameters. Magn Reson Med 79, 2731–2737, doi:10.1002/mrm.26900 (2018). [PubMed: 28862349]
27. Donahue MJ et al. Assessment of lymphatic impairment and interstitial protein accumulation in patients with breast cancer treatment-related lymphedema using CEST MRI. Magnetic Resonance in Medicine 00, n/a-n/a, doi:10.1002/mrm.25649 (2015).

28. Zou L et al. The incidence and risk factors of related lymphedema for breast cancer survivors post-operation: a 2-year follow-up prospective cohort study. Breast Cancer 25, 309–314, doi:10.1007/s12282-018-0830-3 (2018). [PubMed: 29397555]
29. Rautiainen J et al. Effect of collagen cross-linking on quantitative MRI parameters of articular cartilage. Osteoarthritis Cartilage 24, 1656–1664, doi:10.1016/j.joca.2016.04.017 (2016). [PubMed: 27143363]
30. Hoffner M, Peterson P, Mansson S & Brorson H Lymphedema Leads to Fat Deposition in Muscle and Decreased Muscle/Water Volume After Liposuction: A Magnetic Resonance Imaging Study. Lymphat Res Biol, doi:10.1089/lrb.2017.0042 (2017).
31. Spalek M Chronic radiation-induced dermatitis: challenges and solutions. Clin Cosmet Investig Dermatol 9, 473–482, doi:10.2147/CCID.S94320 (2016).
32. Lee BB et al. IUA-ISVI Consensus for diagnosis guideline of chronic lymphedema of the limbs. International Angiology 34, 311–332 (2015). [PubMed: 24699525]
33. Pfister C, Dawzcynski H & Schingale FJ Sodium selenite and cancer related lymphedema: Biological and pharmacological effects. J Trace Elem Med Biol 37, 111–116, doi:10.1016/j.jtemb.2016.05.005 (2016). [PubMed: 27267968]
34. Scaffidi M et al. Early rehabilitation reduces the onset of complications in the upper limb following breast cancer surgery. Eur J Phys Rehabil Med 48, 601–611 (2012). [PubMed: 22510674]
35. Ezzo J et al. Manual lymphatic drainage for lymphedema following breast cancer treatment. Cochrane Database Syst Rev, CD003475, doi:10.1002/14651858.CD003475.pub2 (2015). [PubMed: 25994425]
36. Tan IC et al. Assessment of lymphatic contractile function after manual lymphatic drainage using near-infrared fluorescence imaging. Arch Phys Med Rehabil 92, 756–764 e751, doi:10.1016/j.apmr.2010.12.027 (2011). [PubMed: 21530723]
37. Aldrich MB et al. Seeing it through: translational validation of new medical imaging modalities. Biomed Opt Express 3, 764–776, doi:10.1364/BOE.3.000764 (2012). [PubMed: 22574264]
38. dos Santos Crisostomo RS, Candeias MS, Ribeiro AM, da Luz Belo Martins C & Armada-da-Silva PA Manual lymphatic drainage in chronic venous disease: a duplex ultrasound study. Phlebology 29, 667–676, doi:10.1177/0268355513502787 (2014). [PubMed: 23989970]
39. Crisostomo RS, Candeias MS & Armada-da-Silva PA Venous flow during manual lymphatic drainage applied to different regions of the lower extremity in people with and without chronic venous insufficiency: a cross-sectional study. Physiotherapy 103, 81–89, doi:10.1016/j.physio.2015.12.005 (2017). [PubMed: 27083323]
40. Sedger LM et al. Lipidomic Profiling of Adipose Tissue Reveals an Inflammatory Signature in Cancer-Related and Primary Lymphedema. PLoS One 11, e0154650, doi:10.1371/journal.pone.0154650 (2016). [PubMed: 27182733]
41. Randolph GJ & Miller NE Lymphatic transport of high-density lipoproteins and chylomicrons. J Clin Invest 124, 929–935, doi:10.1172/JCI71610 (2014). [PubMed: 24590278]
42. Zhang J, Zhu W, Tain R, Zhou XJ & Cai K Improved Differentiation of Low-Grade and High-Grade Gliomas and Detection of Tumor Proliferation Using APT Contrast Fitted from Z-Spectrum. Mol Imaging Biol 20, 623–631, doi:10.1007/s11307-017-1154-y (2018). [PubMed: 29313159]
43. Zaiss M et al. Downfield-NOE-suppressed amide-CEST-MRI at 7 Tesla provides a unique contrast in human glioblastoma. Magn Reson Med 77, 196–208, doi:10.1002/mrm.26100 (2017). [PubMed: 26845067]
44. Zhou J et al. Differentiation between glioma and radiation necrosis using molecular magnetic resonance imaging of endogenous proteins and peptides. Nat Med 17, 130–134, doi:10.1038/nm.2268 (2011). [PubMed: 21170048]
45. Xu J et al. On the origins of chemical exchange saturation transfer (CEST) contrast in tumors at 9.4 T. NMR Biomed 27, 406–416, doi:10.1002/nbm.3075 (2014). [PubMed: 24474497]
46. Zu Z Toward more reliable measurements of NOE effects in CEST spectra at around −1.6 ppm (NOE (−1.6)) in rat brain. Magn Reson Med 81, 208–219, doi:10.1002/mrm.27370 (2019). [PubMed: 30058128]

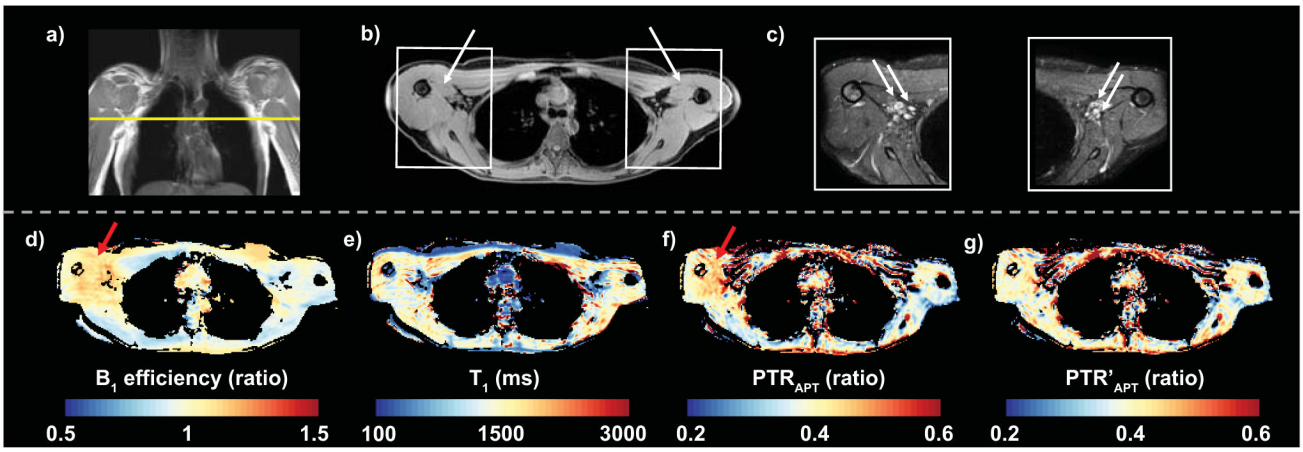

Figure 1. Multi-modal imaging of the axilla.

a) Multi-modal imaging of the upper extremities at the level of the axilla (dashed line depicts transverse image location) is shown in a healthy female volunteer. **b)** Regions of interest were segmented in the medial arm muscle (arrows) adjacent to the axillary region. **c)** High-resolution T_2 weighted images depict the axillary lymph nodes (arrows) and surrounding fat and muscle tissue. Quantitative mapping of **d)** B_1 *efficiency* (ratio), **e)** T_1-relaxation time (ms), and CEST metrics including **f)** PTR_{APT} (ratio) and **g)** PTR'_{APT} (ratio) corrected for B_1 *efficiency* was performed in an identical field of view. In regions of B_1 *efficiency* ratio >1 (red arrows), PTR'_{APT} compared to PTR_{APT} maps demonstrate reduced heterogeneity and greater symmetry between left and right arms after correction in this healthy volunteer.

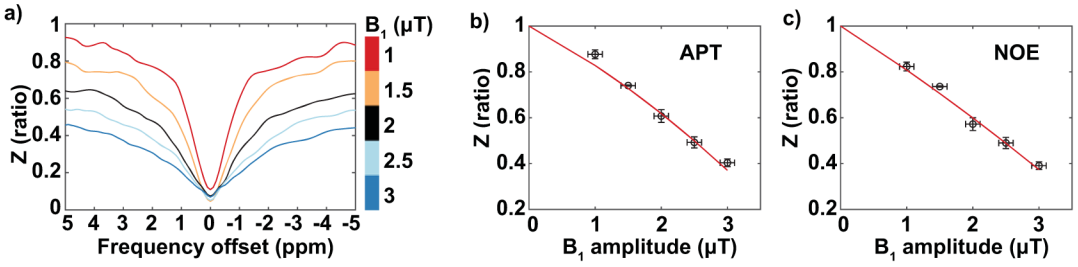

Figure 2. B_1 dispersion experiments.

a) Z-spectra are plotted as a function of saturation frequency offset ($\Delta\omega$, in units of *ppm*) from water resonance ($\Delta\omega = 0$ *ppm*) for varying nominal B_1 amplitudes (1 μT to 3 μT) acquired in the arm muscle of a healthy female volunteer. **b-c)** Z-values in the range of APT and NOE are plotted as a function of B_1 amplitude, and fit to a second order polynomial (red line). Error bars represent one standard deviation of the parameter within the axillary ROI.

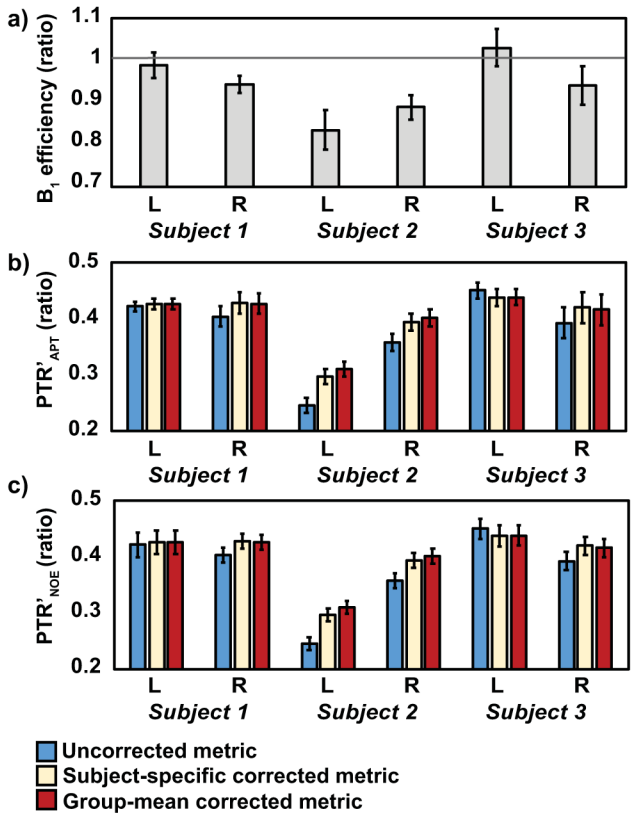

Figure 3. B_1 correction using subject-specific or group-mean correction factors in three healthy volunteers.

a) The acquired B_1 *efficiency* in the left (L) or right (R) upper extremities of three subjects (1, 2, or 3) is compared to the solid line denoting the nominal transmit power. Correction for B_1 inhomogeneity was applied to PTR in the range of **b)** APT and **c)** NOE. B_1 correction using subject-specific or group-mean correction factors similarly adjusts PTR metrics compared to uncorrected metrics. Error bars represent one standard deviation of the parameter within the axillary ROI.

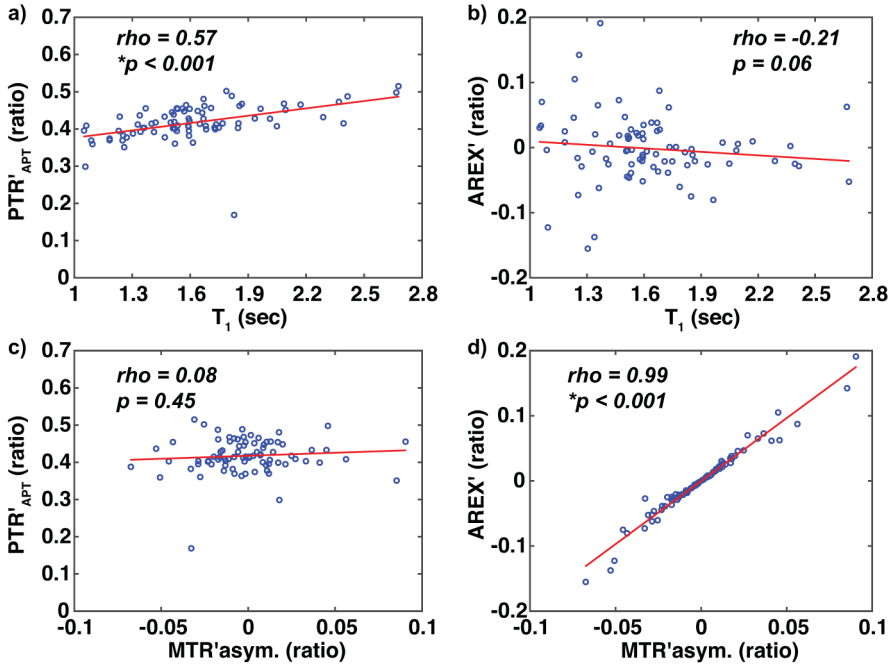

Figure 4. Relationships between imaging metrics.

a) PTR'$_{APT}$ has a significant, positive relationship with T_1 relaxation time. **b)** AREX' demonstrates a weak, inverse relationship with T_1 relaxation time as expected. **c)** There is a weak relationship between CEST metrics PTR'$_{APT}$ and MTR'asymmetry (MTR'asym.), which measure different features of the z-spectrum. d) CEST metrics AREX' and MTR'asymmetry have a significant, positive relationship, and both measure the relative amount of APT compared to NOE effects. Spearman's (rho) and significance criteria *p<0.05 are displayed.

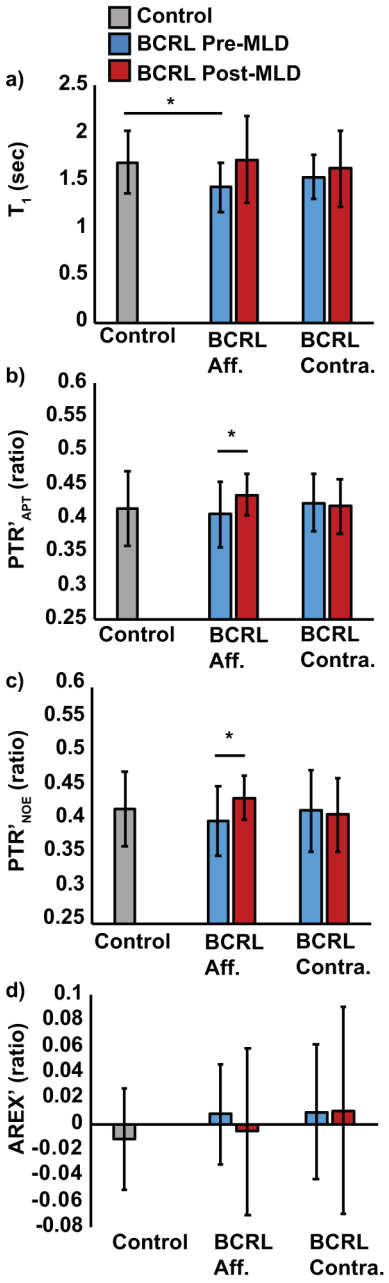

Figure 5. CEST metrics and T_1 relaxation time.

CEST metrics and T_1 relaxation time were evaluated in the deep arm muscle of participants with BCRL (n=12) in the affected (aff.) and contralateral (contra.) axilla, compared to healthy age- and BMI-matched female controls (n=34 including left and right arms); participants were evaluated pre- and post-MLD (manual lymphatic drainage) therapy. **a)** T_1 relaxation time is significantly different in the deep axilla between controls and participants with BCRL on the affected, but not contralateral, side. Following MLD therapy to the affected arm, **b)** PTR'$_{APT}$ and **c)** PTR'$_{NOE}$ were significantly increased in the affected arm compared to baseline imaging. **d)** AREX' is less sensitive than PTR metrics to BCRL status or therapeutic modifications, owing to increased variability and limited dynamic range.

*Two-sided $p<0.05$ required for significance. Error bars represent one standard deviation from the group mean.

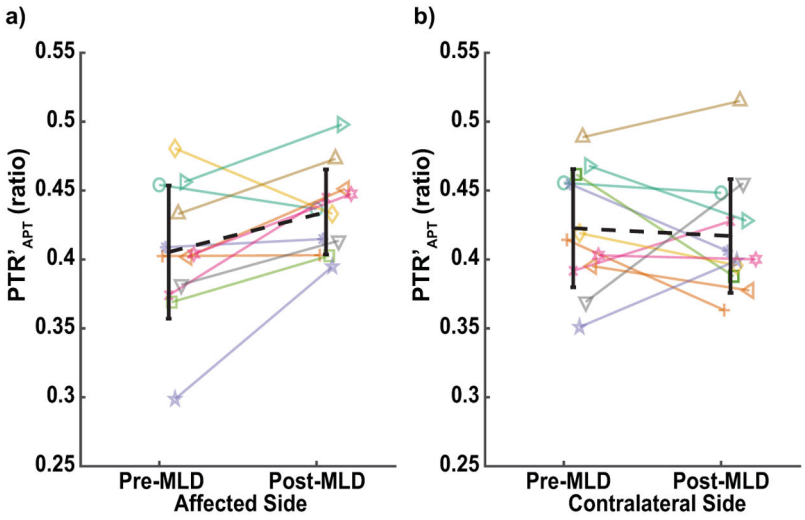

Figure 6.

Change in PTR'_{APT} in the **a)** affected and **b)** contralateral arms pre- and post-MLD therapy is demonstrated for each BCRL participant with a unique line color and symbol combination. The group mean change is represented by the black, dashed line on each graph. Group mean PTR'_{APT} was significantly increased in the affected arm compared to baseline imaging (p=0.02) but not in the contralateral arm (p=0.68).

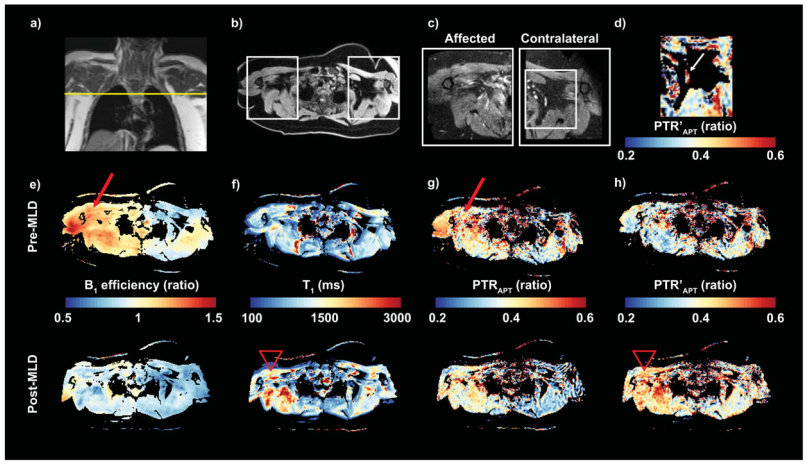

Figure 7.

a) A 47 year old female with Stage 0 BCRL and BMI 45.5 kg/m^2 was imaged in the axillary region before and after MLD therapy. Fifteen months prior to this scan, she had a right modified radical mastectomy and 27 lymph nodes removed with the pathology report indicating no lymph node metastasis. She underwent radiation therapy, and neoadjuvant and adjuvant chemotherapy. **b-c)** Transverse views of both arms were acquired at the level of the axilla using Dixon and high spatial-resolution T_2-SPAIR imaging. Fewer remaining lymph nodes are observed in the affected (right side) compared to contralateral (left side) axilla following surgery. **d)** A PTR'$_{APT}$ parameter map is provided in the contralateral axilla where APT signal is observed in an intact lymph node (arrow). **e)** Parameter maps show B_1 inhomogeneities (arrow) that are asymmetric between right and left sides. **f)** T_1 relaxation is corrected for B_1 *efficiency*, and reveals elevated T_1 on the affected side post-MLD compared to pre-MLD therapy (arrow head). **g)** PTR$_{APT}$ contrast pre- and post-MLD appears elevated on the affected side, however PTR$_{APT}$ contrast corresponds to regions of B_1 inhomogeneity (arrow) and potentially differences in T_1 relaxation post-MLD. **h)** After B_1 correction, the effect of MLD therapy is visualized with reduced artifact from B_1 inhomogeneity. Post-MLD measurement of PTR'$_{APT}$ increases in the affected axillary region compared to pre-MLD measurement (arrow head), consistent with MLD therapy that is applied to the affected side.

Table 1.

Demographic and clinical features of participants with unilateral breast cancer treatment-related lymphedema (BCRL) of the upper extremities.

Patient ID	Age (years)	BMI (kg/m^2)	BCRL Surgical Side (R=1; L=0)	BCRL Stage	Number of LNs removed	Radiation (Yes=1; No=0)	Neo-adjuvant (Yes=1; No=0)	Adjuvant (Yes=1; No=0)
1	55	31.0	1	2	22	1	0	1
2	54	22.5	1	2	21	0	0	1
3	55	34.9	1	2	15	0	0	1
4	47	45.5	1	0	27	1	1	1
5	41	34.2	1	1	15	0	1	1
6	53	32.9	0	1	5	1	0	1
7	48	36.7	0	2	18	1	0	1
8	57	21.6	0	1	21	1	0	1
9	33	30.9	1	2	24	1	1	1
10	77	22.3	1	2	16	1	0	1
11	59	25.3	1	1	19	1	1	1
12	49	28.4	0	2	8	1	0	1
Mean	52.3	30.5	0.67	1.3	17.6	0.75	0.33	1
Standard deviation	10.7	7.0	0.49	0.89	6.3	0.45	0.49	0

Table 2.

Relationship between imaging metrics and demographic parameters in female control participants, or clinical risk factors in participants with BCRL. Spearman's correlation tests were performed between the independent variable and each imaging metric, and Spearman's rho reported.

			Dependent Variable		
Cohort	**Number of Observations**	**Independent Variable**	***PTR'*$_{APT}$ (ratio)**	***AREX'* (ratio)**	**T_1 (sec)**
Controls	34	BMI	**−0.37** *	**−0.36** *	−0.09
Controls	34	Age	0.002	−0.29	0.036
Patients	24	BCRL Stage	**0.48***	−0.06	0.35
Patients	24	Number of LNs†	−0.13	−0.18	−0.04

* values in bold indicate $p<0.05$ significance criteria met

† Number of lymph nodes removed or dissected from the axillary region